PAPER • **OPEN ACCESS**

Potential eutectic accumulation in single crystal turbine blade due to geometry effect: a numerical study

To cite this article: H J Zhang *et al* 2023 *IOP Conf. Ser.: Mater. Sci. Eng.* **1274** 012026

Potential eutectic accumulation in single crystal turbine blade due to geometry effect: a numerical study

H J Zhang[1], X S Liu[2], D X Ma[2], A Ludwig[1], A Kharicha[1], M H Wu[1,*]

[1] Chair for Simulation and Modelling of Metallurgy Processes, Department of Metallurgy, University of Leoben, A-8700 Leoben, Austria

[2] Central South University, Powder Metallurgy Research Institute, Changsha, 410083, China

* Corresponding author: menghuai.wu@unileoben.ac.at

Abstract. Inhomogeneous distribution of the eutectic phase in single crystal (SC) turbine blades is detrimental to its mechanical properties. In a recent publication, it was reported that an accumulation of eutectics was observed on the upper surface of solidification units (e.g. shroud of a turbine blade), whereas fewer eutectics were detected at the bottom. This kind of casting defect brings a huge challenge to the production of turbine blades since the accumulated eutectics cannot be dissolved completely by heat treatment. A sample with three pairs of platforms/shrouds was designed to study the geometry effect on eutectic accumulation. In the current study, the simulation was performed by coupling ProCAST with our previously developed multiphase volume-average solidification model. In the first step, the thermal field including radiation in the furnace and heat conductivity in the casing and mould was calculated via ProCAST. Then, the obtained temperature profiles were set as thermal boundary conditions of the casting to predict the eutectic accumulation and formation of freckles. Based on the simulation results, convective plumes arising from the thermosolutal buoyancy transport solute-enriched liquid upward, which causes the solute pile-up and the final eutectic accumulation at the top surface in each platform. Freckles accompanied with eutectic accumulation was also observed at the corner of the sample. The calculated inhomogeneous distribution of the eutectics agrees well with experimental observations. Knowledge about the geometrical effect on eutectic accumulation is extended.

1. Introduction

The single-crystal (SC) turbine blades fabricated from the Ni-based superalloys have been widely used for aero-engines and industrial gas turbines, because of the high strength, microstructural stability, and corrosion resistance of Ni-based superalloys at elevated temperatures [1, 2]. Typically, the SC blades are directionally solidified in the Bridgman furnace, through which the temperature gradient and withdrawal rate can be well controlled. The solidification of the SC blades is starting with the development of the columnar dendrite matrix phase, i.e. γ phase, and the residual liquid is mainly solidified as the γ/γ' eutectic phase and a minor of intermetallic precipitates [3]. A study by Brewster et al. [4] found that a thin layer of γ/γ' eutectics accumulated on the external surface of the casting along the solidification length. This was explained by the contraction of the solid dendritic network, which squeezed the residual solute-enriched liquid into the sample surface area. The addition of refractory element Re was found to enhance the formation of surface γ/γ' eutectics [4, 5]. In a recent publication [6], it was reported that an accumulation of eutectics was observed on the upper surface of solidification units (e.g. shroud/platform of a turbine blade), whereas fewer eutectics were detected at the bottom. This kind of casting defect poses great challenge to the production of turbine blades since the accumulated eutectics cannot be dissolved completely by heat treatment, and an increased solutioning temperature may cause incipient melting [7]. The aggressive mechanical operation prior to heat treatment will pose additional concerns, e.g. inducing recrystallisation and altering the product dimensions [5].

In this paper, the previously developed multiphase volume-average solidification model [8] is employed to simulate the solidification of a sample with three pairs of platforms. To investigate the geometrical effect on the eutectic accumulation, the liquid flow as raised from the thermo-solutal buoyancy and the as-solidified structure was calculated. The calculated distribution of the γ/γ' eutectics is consistent with the experimental observations.

2. Model description and calculation method

The directional solidification (DS) of the SC casting is carried out in a vacuum Bridgman furnace. As shown in Figure 1(a), the configuration of the furnace includes an inducing hot zone on the top and a cold zone with water cooling at the bottom connected by a graphite baffle in the middle, Al_2O_3 shell mould, superalloy casting, chill base, and grain selector. The shell mould is mounted on the chill base, which drives the mould to move during the casting process. To study the geometrical effect, i.e. the abrupt transition of the cross-section, as shown in Figure 1(b), a specifical geometry with three pairs of platforms (H1–H3, S1–S3), which protruded 15.0 mm on each side of the casting, was designed to simplify the complex turbine blades. One narrow side of the casting is facing the heating wall (heating side), while the other side is back to the heating wall (shadow side). Only 1/12 of the furnace, which is occupied by one casting is calculated. Before the casting process, the mould and the superalloy were heated to 1520 ^{o}C, and then the metal melt was poured into the shell mould. The DS of the SC casting was triggered by withdrawing the shell mould from the hot zone to the cold zone at a velocity of 3.0 mm/s. The third generation of the superalloy was used for this study. Its main compositions are presented in Table I.

Table I. The main composition of the superalloy.

Elements	Ni	Ta	Cr	Al	Co	W	Re	Ti	Mo
Content (wt. %)	base	8.07	3.39	5.69	5.97	6.52	4.89	0.15	0.41

To simplify the simulation, the current multi-element superalloy is treated as eight Ni-X binary alloys with constant liquidus slope (m) and solute partition coefficient (k). The equivalent solute concentration was calculated via $\bar{c}_0 = \sum_{i=1}^{N} c_{0,i}$ [9], in which N denoted the number of solute elements. By means of the same method, the equivalent liquidus slope $\bar{m}$, the equivalent solute partition coefficient $\bar{k}$, and the equivalent solute expansion coefficient $\bar{\beta}_{\mathrm{c}}$ can be evaluated via $\bar{c}_0 \cdot \bar{m} = \sum_{i=1}^{N} m_i c_{0,i}$, $\bar{c}_0 \cdot \bar{m} / \bar{k} = \sum_{i=1}^{N} m_i c_{0,i} / k_i$, and $\bar{c}_0 \cdot (1-\bar{k})\bar{\beta}_{\mathrm{c}} = \sum_{i=1}^{N} c_{0,i}(1-k_i)/\beta_{\mathrm{c}i}$, respectively. The material properties and processing parameters are listed in Table II.

The simulations were performed by coupling the commercial software ProCAST and ANSYS Fluent. As shown in Figure 1(c), in the first step, the thermal field was calculated via ProCAST with the consideration of the radiation in the furnace, the heat conductivity in the casing and the shell mould, and the release of the latent heat during the solidification. The geometry used for the thermal calculation in ProCAST is shown in Figure 1(a). It should be mentioned that the effect of the liquid flow on the thermal field was not considered due to its low intensity. Then, the obtained temperature profiles on the casting surface were extracted and set as thermal boundary conditions of the casting for calculation of flow-solidification interaction. Only the casting domain, Figure 1(b), was solved using our previously developed multiphase volume-average solidification model [8] to predict the eutectic accumulation and formation of freckles. Since the nature of the single crystal growth, only the liquid melt and the solid columnar dendrites were considered here with their volume fractions equal to unit, i.e. $f_l + f_c = 1$. The columnar dendrites can only start to grow from the bottom of the domain, which is connected to the top of the grain selector. The no-slip boundary condition was applied to all walls, and the alloy was assumed to be incompressible with constant density and viscosity.

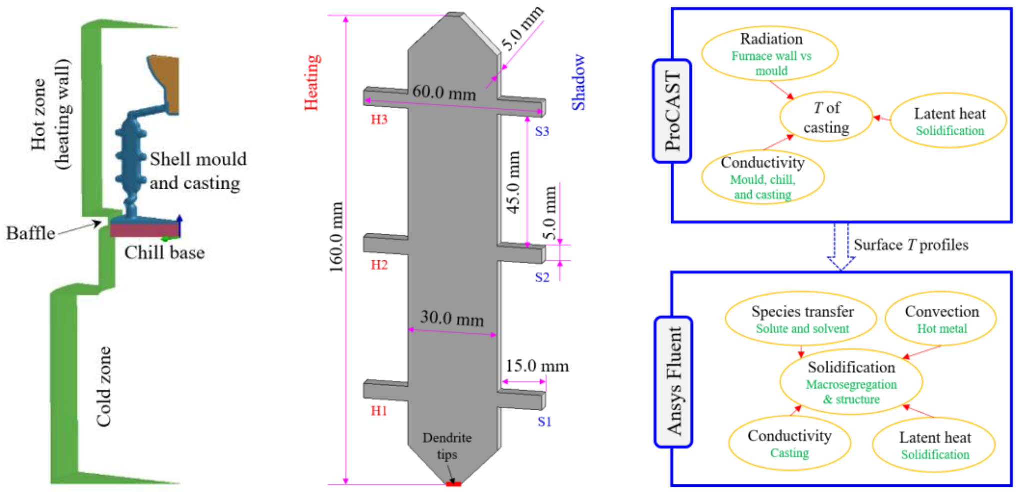

(a) (b) (c)

Figure 1. (a) Layout of the Bridgman furnace and the assemble of the casting; (b) Dimension of the casting domain; (c) Sketch of the calculation strategy.

Table II. Material properties and processing parameters [9–12].

Properties/parameters	Symbol	Units	Values
Thermophysical			
Specific heat of the alloy	$c_{p,l}$ $c_{p,s}$	$J \cdot kg^{-1} \cdot K^{-1}$	500.0
Latent heat	Δh_f	$J \cdot kg^{-1}$	2.4×10^5
Liquid diffusion coefficient	D_l	$m^2 \cdot s^{-1}$	3.6×10^{-9}
Liquid thermal conductivity	k_l	$W \cdot m^{-1} \cdot K^{-1}$	33.5
Solid thermal conductivity	k_s	$W \cdot m^{-1} \cdot K^{-1}$	24.6
Thermal expansion coefficient	β_T	K^{-1}	-1.16×10^{-4}
Solutal expansion coefficient	$\bar{\beta}_c$	$wt.\%^{-1}$	–0.228
Density	ρ	$kg \cdot m^{-3}$	7646.0
Viscosity	μ_l	$kg \cdot m^{-1} \cdot s^{-1}$	4.9×10^{-3}
Thermodynamic			
Eutectic temperature	T_{eut}	K	1627.0
Liquidus slope	$\bar{m}$	$K (wt. \%)^{-1}$	−1.145
Equilibrium partition coefficient	$\bar{k}$	-	0.57
Primary dendritic arm spacing	λ_1	μm	500.0
Melting point of the solvent	T_f	K	1728.0
Others			
Initial concentration	$\bar{c}_0$	wt.%	35.09
Initial temperature	T_0	K	1773.0
Withdrawal velocity	v	mm/min	3.0

3. Simulation results and discussions

3.1, Comparison of the temperature field

The calculated temperature field in the Bridgman furnace is shown in Figure 2(a). A positive temperature gradient is formed along the casting direction. Since the heating and cooling by the furnace wall above and below the baffle, respectively, the temperature gradient of the shell mould on the left side (heating side) is higher, resulting in a narrower mushy zone on this side, Figure 2(b). The temperature profiles along two vertical lines, as marked in Figure 2(b) are plotted in Figure 2 (c). Above the baffle, the temperature on the heating side of the casting can be 13 K higher than that on the right side, while below the baffle, it is about 17K lower on the heating side. From Figure 2(c), it can also be seen that the calculated temperature profiles by these two different solvers are identical, which ensure the credibility of the thermal boundary conditions that are used for the flow calculation.

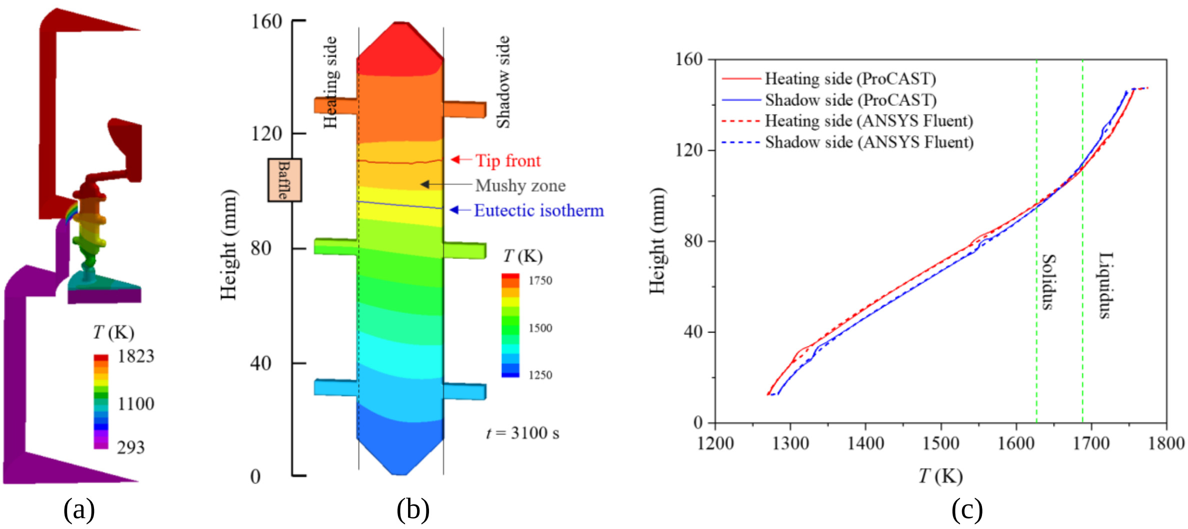

Figure 2. Calculated temperature results: (a) *T* filed in the Bridgman furnace; (b) *T* filed on the casting surface with the identification of the solidification front and the eutectic isotherm; (c) comparison of *T* profiles along the two vertical lines (as marked in Figure 2(b)) calculated by ProCAST and ANSYS Fluent.

3.2, Flow pattern and solidification sequence

During the solidification of the current SC casting, the liquid flow is driven by the thermal-solutal buoyancy. In the bulk liquid of the casting, due to the nearly homogeneous solute concentration, the liquid convection is dominated by the thermal buoyancy. As shown in Figure 3(a), a clockwise flow up to the strength of 3 mm/s is generated in the top part of the casting domain. Some isolated vortices, as indicated by the light blue vectors in Figure 3(a), can be found in the platforms. The flow in these platforms is more than one order of magnitude lower (~ 0.1 mm/s) than the flow in the main casting. In the mushy zone, the solute rejection due to the solidification causes the density inversion, i.e. the solutal buoyancy exceeds the thermal effect. The lighter solute-enriched liquid enclosed in those convective plumes floats upward, as indicated by the green vector on those plumes in Figure 3(a). Due to the blowing effect of the main flow (black vectors) in the bulk liquid, the plumes tilt to the left.

The solidification sequence when the solidification front passes the first pair of platforms (S1 and H1) is presented in Figs. 3(b)–(e). Before the solidification front reaches S1, although the melt in S1 has been sufficiently undercooled, it does not solidify until the solidification front advances there. Once the dendrites develop to S1, the side branches extend quickly to the right side and the alloy solidifies rapidly, which causes the convex solidification front in S1. The small vortex in S1 persists its previous flow pattern that is presented in Figure 3(a). With the solidification of the casting, as shown in the zoom-in view of Figure 3(c), local density inversion due to the solute pile-up in the interdendritic region drives the upward flow (~ 0.6mm/s) in S1. Some short plumes, as marked by the green iso-surfaces, can also be seen above the solidification front. Although S1 is connected to the casting, since the fact that the narrow gate at the connection has been partially solidified, the liquid is difficult to flow out of S1. The local circulation in S1 transports more and more solute-enriched liquid to the top surface, which causes the final eutectic accumulation there. The solute diffusion due to the solute concentration gradient is also one possible mechanism for the eutectic accumulation on the top, but plays a small role compared to the convective effect. The solidification in the heating side, H1, is a bit different from S1. As shown in Figure 3(d), a flat solidification front was observed in H1. This can be understood with the assist of Figure 2. At the solidification front, the liquid on the heating side is warmer than the liquid on the shadow side. There is no intensive undercooling like S1. When the dendrites develop to H1, the side branches can extend gradually to the left side. The flow and solidification in a later moment (Figure 3(e)) are similar to that of Figure 3(c). The local circulation leads to the enrichment of the residual solute-enriched liquid at the top surface of H1, and hence the final eutectic accumulation. Freckles are also observed on this casting. As displayed in Figure 3(f), all freckles are formed at the four vertical corners of the casting, and the shadow side is prone to form freckles. Accumulation of eutectic was also found in these freckle areas, which can be seen through the zoom-in view in Figure 3(f). Formation mechanism and quantitative comparison with experiments of the freckles will be made in our subsequent journal paper.

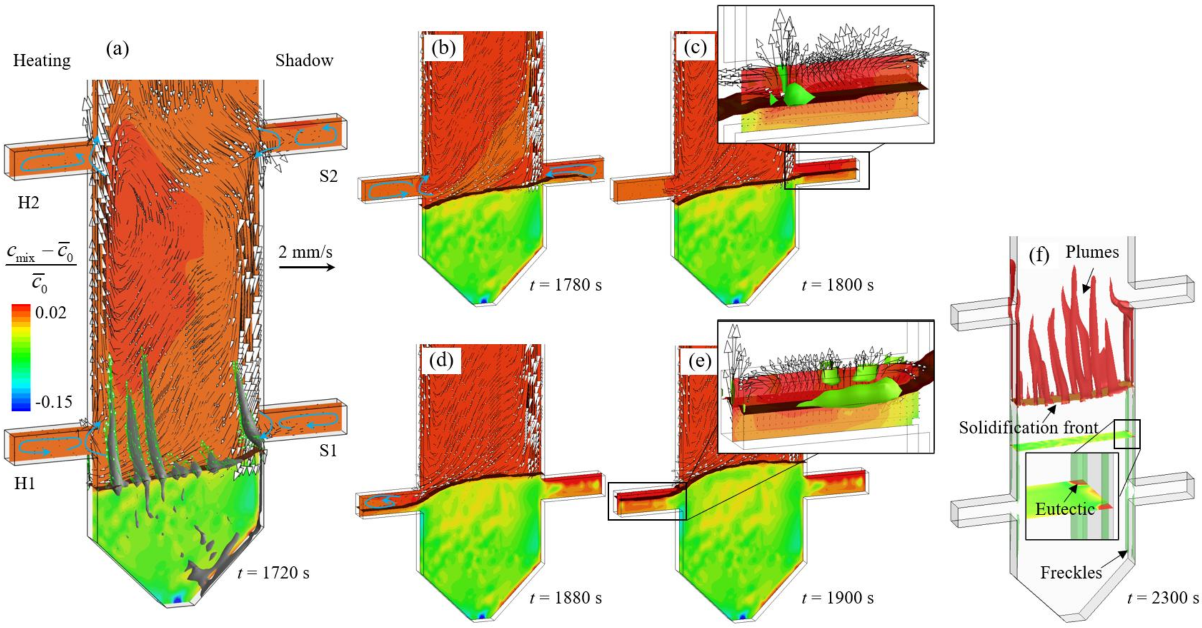

Figure 3. The calculated flow pattern and solidification sequence of the sample. (a) Contour of segregation index $(c_{\mathrm{mix}} - \bar{c}_0)/\bar{c}_0$ in the central section overlaid by the black vectors of liquid velocity $\vec{u}_1$; the solidification front is indicated by a horizontal iso-surface, and the convective plumes are denoted by the vertical columns overlaid by the green vectors of $\vec{u}_1$. (b)-(e) Contour of $(c_{mix} - \bar{c}_0)/\bar{c}_0$ in the central section overlaid by the black vectors of $\vec{u}_1$; the horizontal iso-surface indicates the solidification front. (f) Distribution of plumes over the solidification front and freckles below the solidification front.

3.3, Comparison with experiments

The calculated final distribution of the eutectics (f_{eut}) on the central section of the casting is presented in Figure 4(a). A quantitative analysis to show the evolution of f_{eut} from the bottom to the top of these six platforms is made in Figure 4 (b). Specifically, a thin eutectic accumulated layer (~1.5 mm) can be observed near the top surface of each platform, while a relatively low f_{eut} at the bottom of them. Based on the zoom-in view of Figure 4(a), the current simulation results agree well with the experimental observation [6]. Additionally, more eutectics form in the platforms at a higher position. The same tendency was also observed in the main casting. From point A， B to C, f_{eut} is equal 9.5%, 11.6%, 20.1%, respectively. A eutectic concentrated region can also be seen at the top of the casting. As shown in Figure 3(a), the convective plumes transport solute-enriched liquid that is rejected from the interdendritic region into the up-bulk liquid and raise the solute concentration of the unsolidified liquid, which is responsible for increasing f_{eut} along the casting direction.

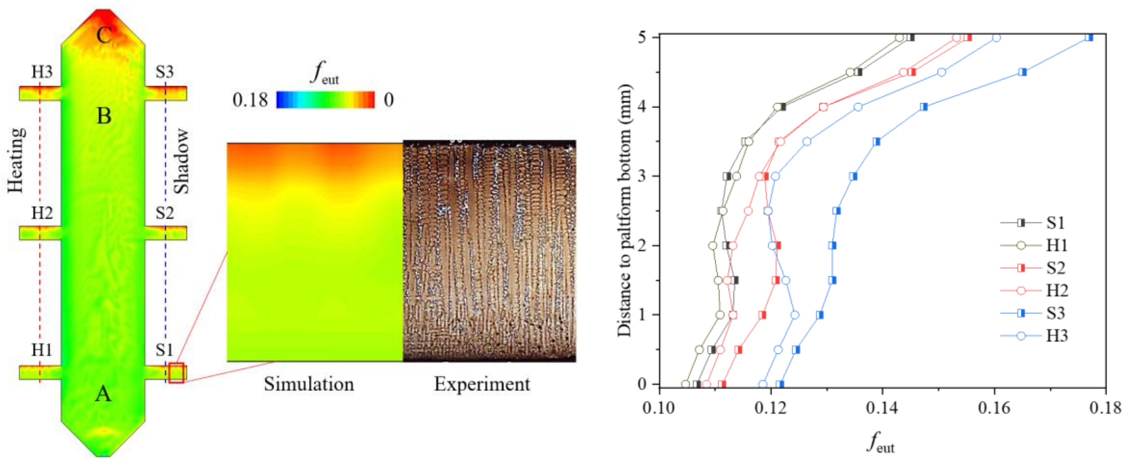

(a) (b)

Figure 4. Validation of the calculated f_{eut}. (a) Distribution of f_{eut} on the central section of the casting, and a zoom-in view to show the local solidification structure. (b) Evolution of f_{eut} from the bottom to the top of these platforms along the dash lines in **Figure 4(a)**.

4. Conclusions

The Potential eutectic accumulation in SC turbine blade due to geometry effect was numerically studied based on a special casting with three pairs of platforms. The simulation was performed by coupling ProCAST with a volume-average multiphase solidification model. Based on the current simulation results, the convective plumes arising from the thermosolutal buoyancy transport the solute-enriched liquid upward. During the solidification, the enriched liquid can hardly flow out of the partially solidified platform through the narrow gate at the connection. The solute-enriched liquid finally solidified as a thin layer (~1.5 mm) of eutectic phase at the top surface. The convective plumes also cause the increased f_{eut} along the casting direction in the main casting, and the eutectic concentrated area at the top of the casting. Freckles accompanied with eutectic accumulation were observed at the four corners of the sample.

5. Acknowledgement

This work was financially supported by the Austrian Science Fund in the framework of the FWF-NKFIN joint project (FWF, I4278-N36).

6. References

[1] D. Ma and A. Bührig-Polaczek: *Metall. Mater. Trans. A*, 2014, vol. 45, pp. 1435–44.
[2] G.P. Sabol and R. Stickler: *Phys. status solidi*, 1969, vol. 35, pp. 11–52.
[3] K. Cao, W. Yang, J. Zhang, C. Liu, P. Qu, H. Su, J. Zhang, and L. Liu: *J. Mater. Res. Technol.*, 2021, vol. 11, pp. 474–86.
[4] L. Cao, L. Yao, Y. Zhou, T. Jin, and X. Sun: *J. Mater. Sci. Technol.*, 2017, vol. 33, pp. 347–51.
[5] L. Cao, Y. Zhou, T. Jin, and X. Sun: *J. Mater. Sci. Technol.*, 2017, vol. 33, pp. 1308–13.
[6] D. Ma, Y. Zhao, W. Xu, L. Pi, and Z. Li: *Acta Met. Sin*, 2021, vol. 57, pp. 1539–48.
[7] G. Brewster, H.B. Dong, N.R. Green, and N. D'Souza: *Metall. Mater. Trans. B*, 2008, vol. 39, pp. 87–93.
[8] M. Wu, A. Ludwig, and A. Kharicha: *Metals (Basel).*, 2019, vol. 9, p. 229.
[9] N. Ren, J. Li, C. Panwisawas, M. Xia, H. Dong, and J. Li: *Acta Mater.*, 2021, vol. 206, p. 116620.
[10] 11 S.D. Felicelli, D.R. Poirier, and J.C. Heinrich: Metall. *Mater. Trans. B*, 1998, vol. 29, pp. 847–55.
[11] P.N. Quested, R.F. Brooks, L. Chapman, R. Morrell, Y. Youssef, and K.C. Mills: *Mater. Sci. Technol.*, 2009, vol. 25, pp. 154–62.
[12] D. Szeliga: Metall. *Mater. Trans. B*, 2018, vol. 49, pp. 2550–70.